Journal of Power Sources 185 (2008) 1454–1464

Contents lists available at ScienceDirect

Journal of Power Sources

journal homepage: www.elsevier.com/locate/jpowsour

Cycle life evaluation of 3 Ah $Li_xMn_2O_4$-based lithium-ion secondary cells for low-earth-orbit satellites
II. Harvested electrode examination

Shelley Brown[a,*], Keita Ogawa[b], Youichi Kumeuchi[c], Shinsuke Enomoto[c], Masatoshi Uno[d], Hirobumi Saito[d], Yoshitsugu Sone[d], Daniel Abraham[e], Göran Lindbergh[a]

[a] School of Chemical Science and Engineering, Department of Chemical Engineering and Technology, Teknikringen 42, Royal Institute of Technology, Stockholm SE-100 44, Sweden
[b] Advanced Engineering Services Co., Ltd., 1-6-1 Takezono, Tsukuba, Ibaraki 305-0032, Japan
[c] NEC-Tokin Corporation, 1120 Shimokuzawa, Sagamihara, Kanagawa 229-1198, Japan
[d] Japan Aerospace Exploration Agency, Institute of Space and Astronautical Science, 3-1-1 Yoshinodai, Sagamihara, Kanagawa 229-8510, Japan
[e] Chemical Engineering Division, Argonne National Laboratory, 9700 South Cass Avenue, Argonne, IL 60439, USA

ARTICLE INFO

Article history:
Received 11 May 2008
Received in revised form 6 July 2008
Accepted 13 July 2008
Available online 5 August 2008

Keywords:
Lithium-ion
LEO satellite
Ageing
Porous electrode
Impedance
Three-electrode measurement

ABSTRACT

Lithium-ion batteries are a candidate for the energy storage system onboard low-earth-orbit satellites. Terrestrial experiments are able to capture the performance degradation of cells in orbit, therefore providing the opportunity for lifetime investigations. The lifetime performance of 3 Ah commercial $Li_xMn_2O_4$-based pouch cells was evaluated in a matrix of different cycling depths-of-discharge (DODs: 0, 20, 40%) and temperatures (25, 45 °C). Aged cells were disassembled and the electrochemical performance of harvested electrodes investigated with two- and three-electrode pouch cells. The positive electrode had a larger decrease in capacity than the negative electrode. Both the positive and negative electrode contributed to the increase of cell impedance measured at high states-of-charge (SOCs). The data at low SOCs indicated that the increase of cell impedance was associated with the positive electrode, which showed a significant increase in the magnitude of the high-frequency semi-circle. This SOC-dependence was observed for cells cycled for either extended periods of time or at higher temperatures with a 40% DOD swing. Low-current cycling of positive electrodes revealed a change in the second potential plateau, possibly reflecting a structural change of the $Li_xMn_2O_4$. This could impact on the electrode kinetics and provide a possible explanation for the SOC-dependent change of the impedance.

1. Introduction

Lithium-ion batteries are attractive energy storage devices for low-earth-orbit (LEO, 500–1000 km above the earth) satellites due to their high energy density, high working voltage, low self-discharge and potential flexibility with laminated cell packaging [1]. A satellite in LEO typically experiences 65 min of sunshine during which time the battery is recharged via the solar cells, followed by 35 min of eclipse where the battery meets the electrical demands of the mission. In order to achieve a 5- year LEO mission life (30,000 cycles without interruption), lithium-ion cells must be operated under moderate conditions, which includes a shallow depth-of-discharge (typically between 20 and 40%) and a reasonable temperature range (10–25 °C) [1–10]. Of key interest to satellite power systems engineers is how to manage a particular lithium-ion battery chemistry, with a specific cell design, in order to maximise the cycle life.

One of the candidate lithium-ion technologies for LEO satellites utilises a manganese spinel intercalation material as the active component of the porous positive electrode. In comparison with other typical positive electrode materials, manganese spinel is promising because it is inexpensive, is environmentally friendly and has good safety characteristics [11]. Typically synthesised as a highly crystalline product at ~ 750 °C, stoichiometric $LiMn_2O_4$ spinel provides a three-dimensional interstitial space for lithium-ion transport with a high voltage (~ 4 V vs Li/Li^+) and a stable cubic (space group $Fd3m$) framework over the whole 4 V compositional range $0 \leq x \leq 1$ in $Li_xMn_2O_4$ [12,13]. Lithium-ions can also be reversibly inserted into $Li_xMn_2O_4$ in the composition range $1 \leq x \leq 2.25$ [14]. This process, however, is a two-phase reaction [15] where the average manganese ion valency falls below 3.5 causing a Jahn–Teller distortion [i.e., the cubic symmetry of $Li[Mn_2]O_4$, in which lithium-ions occupy tetrahedral sites, is reduced to tetragonal $Li_2[Mn_2]O_4$ (space group $F4_1/ddm$), in

* Corresponding author. Tel.: +46 8 7908143; fax: +46 8 108087.
E-mail address: shelleyb@kth.se (S. Brown).

0378-7753/$ – see front matter © 2008 Elsevier B.V. All rights reserved.
doi:10.1016/j.jpowsour.2008.07.071

which the lithium-ions occupy octahedral sites]. The result is an open-circuit potential of 2.96 V vs Li/Li^+ [14] and capacity fade due to structural degradation. This phenomenon restricts the spinel electrode within the limits of the cubic structure with a specific capacity of ~ 120 mAhg^{-1} [13]. Despite the improvement in the room temperature cycle life performance of state-of-the-art $Li_xMn_2O_4$-based lithium-ion batteries, this battery chemistry has received little attention from the space industry for missions, with only one published study on the lifetime performance of 14.6 Ah $Li_xMn_2O_4$battery for LEO satellites [8].

The terrestrial and orbital lifetime performance of commercial 3 Ah pouch cells, based on $Li_xMn_2O_4$technology (NEC-Tokin), has been studied as a part of a JAXA (Japan Aerospace Exploration Agency) program to demonstrate the use of lithium-ion batteries onboard LEO microsatellites [16]. The orbital performance of the pouch cells onboard the microsatellite REIMEI (~ 70 kg, launched August 2005, formerly known as INDEX) was monitored and compared with terrestrial experiments, with the cells found to be unaffected by orbital conditions. A terrestrial lifetime matrix of different cycling DODs (0, 20, 40%) and temperatures (25, 45 °C) was undertaken with periodic reference performance tests. The results indicated that increasing either the depth-of-discharge by 20% or the temperature by 20 °C from the REIMEI base case (DOD 20% 25 °C) had little impact on the degradation of the C/3 discharge capacity. However, a simultaneous increase of ageing temperature (to 45 °C) and depth-of-discharge (to 40%) resulted in significantly larger cell capacity fade. Furthermore, impedance spectra measured for all ageing conditions indicated that the increase was small, manifested mainly in a SOC-dependent increase of the high-frequency semi-circle and a noticeable increase in the high-frequency real axis intercept. In particular, there was a noticeable increase in the width of the high-frequency semi-circle at 25% SOC (the lowest SOC measurement point).

In this study, the 3 Ah commercial pouch cells tested in an accelerated ageing matrix in Part one [16] were removed from testing at specified points in time and the electrodes harvested for further electrochemical measurements. Specially designed two- and three-electrode pouch cell set-ups that recreated, to a reasonable degree, the conditions in the commercial pouch cell were used to measure both the capacity fade and impedance increase at different states-of-charge for both the fresh and aged, positive and negative, electrodes. Electrochemical impedance spectroscopy (EIS) was used to identify the effects of ageing because it discriminates between various subprocesses with different time scales [17,18]. The electrochemical data from the electrodes have been used to shed light on the factors responsible for the observed 3 Ah cell capacity fade and impedance increase. Understanding electrode degradation characteristics of a lithium-ion battery onboard a LEO satellite is an important step in both improving the battery chemistry and developing long-life cells.

2. Experimental

2.1. Accelerated ageing matrix

The 3 Ah commercial pouch cells were supplied by NEC-Tokin (158 Wh kg^{-1}, 340 Wh L^{-1}, 4.1 V upper voltage limit, 3.0 V lower voltage limit). The double-sided positive electrode, consisting of a mixture of active $Li_xMn_2O_4$-based material, carbon additives and binder coated onto an aluminium current collector, was encased in a separator envelope and sandwiched between double-sided negative electrodes, which consisted of a mixture of graphite and binder coated onto a copper current collector (details of thicknesses, loading densities and porosities are proprietary). The liquid electrolyte was 1 M $LiPF_6$EC/DEC (3:7 by wt%) with a few weight percent additives.

Accelerated cycling tests were undertaken at two DODs (20, 40%) and two temperatures (25, 45 °C) at atmospheric pressure. Reference performance tests, including capacity (C/10 and C/3), DC resistance and impedance measurements (four target SOCs: 100, 75, 50 and 25%), were undertaken every 400 cycles, which corresponded to approximately 28 days. Details of the cycling and reference performance test protocols can be found in Part one [16]. The pouch cells were continuously cycled with a LEO regime in an upper SOC-window (i.e., between either 100 – 80% SOC or 100 – 60% SOC), including a 35 min constant current discharge (1.0 A for ΔDOD 20% and 2.0 A for ΔDOD 40%) and a 65 min constant current/constant voltage recharging scheme with 1.5 A and a 4.1 V upper voltage limit. The different portions of the lifetime matrix were started at different times, resulting in 4800 completed cycles at 25 °C DOD 20%, 3400 completed cycles at 25 °C DOD 40%, and 1600 completed cycles for both discharge current loads at 45 °C. Two cells were tested at all conditions except for 25 °C DOD 40%, where six cells were used to allow for frequent removal of cells from testing for disassembly. During the 1 year of lifetime testing at JAXA, two cells were removed from the 25 °C DOD 40% tests (after 1200 and 2200 completed cycles) and one cell was removed after 1200 completed cycles from 45 °C DOD 20% and 45 °C DOD 40% tests. Cells removed from cycling were stored in a fully discharged state at 7 °C prior to disassembly.

2.1.1. Disassembling pouch cells and harvesting electrodes

The aged 3 Ah cells removed from cycling, together with a fresh 3 Ah pouch cell (only subjected to formation cycling by the manufacturer), were carefully disassembled in a dry room. The pouch material was removed and a sheet of the positive and negative electrode harvested from the centre of the battery. Four square (30 mm × 30 mm) samples were cut from each sheet, giving one sample for a three-electrode measurement, one sample for a two-electrode measurement and two samples as reserve in the case of cell failure or future materials analysis. The rectangular samples were double-sided, so the active material was carefully removed from one side by doing the following. Using a scalpel, a small amount of active material was removed from the edges on both sides of the sample. The sample was placed on a piece of paper, and a cloth soaked in 1-methyl-2-pyrrolidone (NMP) was used to very carefully remove the active material from the back side of the electrode. The sample was then placed in a die cutter and a circular electrode with a diameter of 18 mm was punched out. The harvested circular electrodes were washed in dimethyl carbonate (DMC) and carefully dried at 25 °C under reduced pressure. Samples for electrochemical testing were immediately placed into the relevant cell set-up. Reserve samples were placed into sealed plastic bags, which were further encased in a pouch cell that was heat-sealed and placed in a refrigerator at 5 °C.

The harvested samples were labelled and will be referred to as follows for clarity during the article: *p* (positive), *n* (negative), 1 (25 °C DOD 40% 1200 completed cycles), 2 (25 °C DOD 40% 2200 completed cycles), 3 (45 °C DOD 20% 1200 completed cycles), 4 (45 °C DOD 40% 1200 completed cycles) and 5 (fresh electrode).

2.2. Two-electrode measurements of positive and negative electrodes (fresh and aged)

Two-electrode pouch cells were prepared to investigate the electrochemical characteristics of the positive and negative porous electrodes, including charge–discharge behaviour and capacity with different currents. The cells consisted of an electrode assembly inserted into a pouch, with the edges heat-sealed under vacuum.

Table 1
Pouch cell design

Component	Specification
Working porous electrode	18 mm diameter - one-sided
Counter electrode	Lithium foil 25 mm × 30 mm rectangle 0.03 mm thick
Whatman separator	0.260 mm thick 31 mm × 40 mm rectangle
Working electrode tab	aluminium 45 mm × 5 mm (0.1 mm thick) (positive case) nickel 45 mm × 4 mm (0.1 mm thick) (negative case)
Counter electrode tab	nickel 45 mm × 4 mm (0.1 mm thick)
Electrolyte	1 M $LiPF_6$ EC:DEC (3:7 by wt%) 0.75 mL

The details of the electrode assembly, for both positive and negative porous electrode samples, are given in Table 1. The working electrode was either a fresh or aged, positive or negative, circular porous electrode with an 18 mm diameter. The working electrode was contacted with either an aluminium (45 mm × 5 mm × 0.1 mm) or nickel (45 mm × 4 mm × 0.1 mm) current collector strip for the positive and negative sample, respectively. The counter electrode was a rectangular piece of lithium foil (25 mm × 30 mm × 0.03 mm) contacted with a nickel current collector strip (45 mm × 4 mm × 0.1 mm). The electrodes were separated by a rectangular piece of glass microfibre separator (Whatman GF/A: 31 mm × 40 mm × 0.260 mm). A fixed volume (0.75 mL) of liquid electrolyte, 1 M $LiPF_6$EC/DEC (3:7 by wt%), was added with a pipette to the separator layer.

To determine the capacity of fresh and harvested electrodes, the cells were cycled between either 3.0–4.2 V or 0.01–1.5 V for the positive and negative electrode cells, respectively. The cycling protocol for the positive electrode cell involved a constant current/constant voltage charge to the upper voltage limit of 4.2 V, an OCP period of 2 h, a constant current discharge of the cell down to the lower voltage limit of 3.0 V, followed by 2 h at OCP. The cycling protocol for the negative electrode cell involved a constant current/constant voltage discharge down to the lower voltage limit of 0.01 V, an OCP period of 2 h, a constant current charge of the cell up to the upper voltage limit of 1.5 V, followed by 2 h at OCP. These cycling tests were repeated twice at different currents with a multichannel TOSCAT potentiostat: C/10 (2.08 A m^{-2}), C/3 (8.25 A m^{-2}), C/2.7 (9.43 A m^{-2}) and C/1.5 (17.68 A m^{-2}). The C/2.7 and C/1.5 capacity checks were undertaken after calculating the constant current required to either charge 40% of the electrode capacity in 65 min or discharge 40% of the electrode capacity in 35 min, respectively, which were the charge and discharge cycling conditions for majority of the disassembled 3 Ah full cells.

2.3. Three-electrode measurements of positive and negative electrodes (fresh and aged)

A three-electrode set-up was designed and used to investigate the electrochemical behaviour of fresh positive and negative porous electrodes, including: (1) open-circuit potential as a function of SOC with the galvanostatic intermittent titration technique (GITT), (2) capacity with two different currents (providing a basis of comparison with the measured two-electrode capacities), and (3) impedance behaviour at multiple SOCs. The same electrochemical experiments, minus the GITT measurement, were undertaken on aged positive and negative porous electrode samples. A diagram of the three-electrode design is shown in Fig. 1(a). The electrode assembly was similar to that of the two-electrode pouch cell assembly except for the following differences: the working and lithium

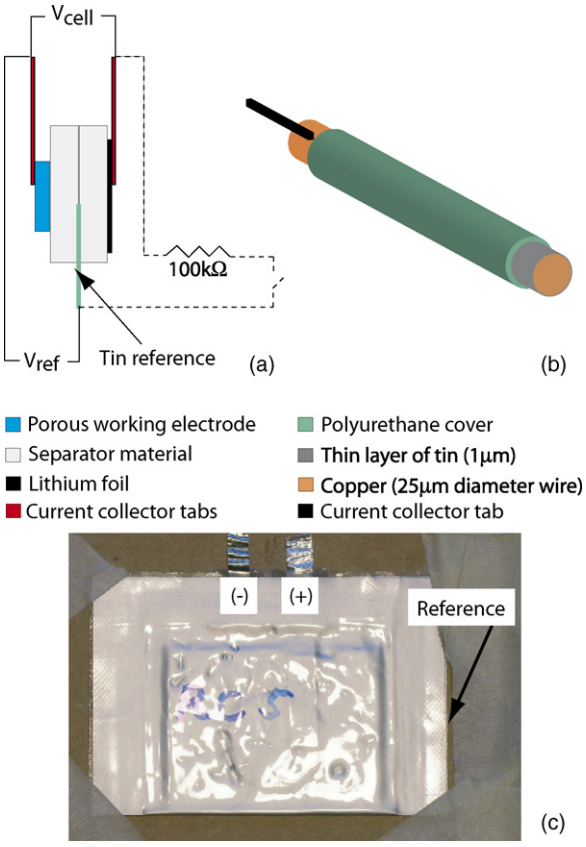

Fig. 1. Three-electrode pouch cell configuration: (a) cell sandwich with demonstration of the placement of the 100 kΩ resistor during reference electrode lithiation, (b) tin reference electrode, and (c) top view of cell (For interpretation of the references to colour in this figure legend, the reader is referred to the web version of the article).

metal counter electrode were separated by two rectangular pieces of glass microfibre separators. Sandwiched between the two separators was a reference electrode based on a lithium–tin alloy and developed in other work [19]. The reference electrode, shown in detail in Fig. 1(b), consisted of a copper wire (25 μm diameter) covered with a thin layer of tin (1 μm thick), with the whole assembly covered with a thin layer of polyurethane. Dipping each end of the reference electrode individually into NaOH solution at 90–94 °C for 2–3 min stripped away a portion of the polyurethane layer, with the end inserted into the three-electrode set-up ~ 5 mm long and the end for soldering ~ 15 mm long. The end inserted into the pouch cell was stripped to allow for lithium to be intercalated into the thin tin layer. The other end of the reference electrode was stripped to allow for a metal tab to be attached with welding in order to provide a good electronic contact. The reference electrode was prepared *in situ* by connecting the counter electrode via a 100 kΩ resistor to the reference electrode for 40 min, followed by 7 h under open-circuit conditions. The potential during the lithiation of the reference electrode was measured with a Solartron 1280 C potentiostat. After 7 h, the reference electrode potential stabilised and remained in such a condition for up to a week. Prior to undertaking three-electrode measurements on aged samples, a fresh prototype cell was assembled and successfully tested.

GITT measurements were conducted on fresh positive and negative electrodes in order to relate electrode potentials to state of charge (SOC). The measurement on the positive electrode involved discharging the cell from 4.2 V vs Li/Li^+ with a C/10 (2.08 A m^{-2}) constant current for 20 min, followed by OCP for 3 h; this routine was repeated 35 times in order to discharge the full electrode

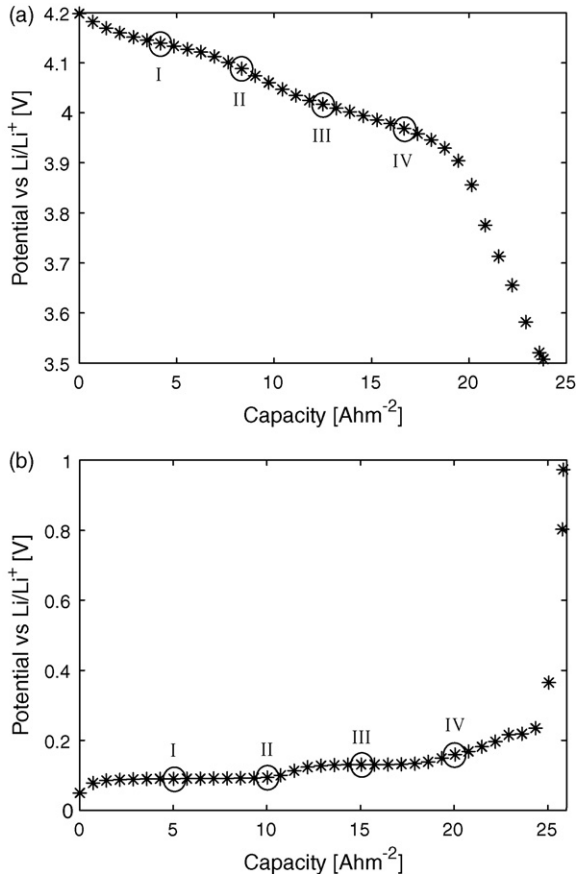

Fig. 2. Results of GITT measurements [C/10 (2.08 A m^{-2}) discharge for 20 min followed by 3 h OCP]: (a) positive electrode; 3.0 V vs Li/Li$^+$ discharge limit, (b) negative electrode; 1.5 V vs Li/Li$^+$ charge limit. Designated measurement SOC points: (I) SOC 80%, (II) SOC 60%, (III) SOC 40%, (IV) SOC 20% (Note: measurement points were chosen to investigate different plateaus, and do not necessarily correspond with the electrode SOC in the 3 Ah full cell).

capacity. The measurement on the negative electrode involved charging the cell from 0.01 V vs Li/Li$^+$ with a C/10 (2.08 A m^{-2}) constant current for 20 min, followed by OCP for 3 h; this routine was repeated 37 times in order to completely delithiate the graphite active material. The GITT data for both the positive and negative electrodes, shown in Fig. 2(a) and (b), respectively, revealed the typical phase changes associated with manganese spinel and graphite chemistries [20].

The capacity of all cells was measured with a multichannel potentiostat (TOSCAT 3000) prior to the impedance measurements. The positive electrode cells were cycled as a two-electrode cell, with the working electrode cable connected to the oxide electrode, and the counter electrode cable connected to the lithium foil. The cells were cycled twice between 3.0 and 4.2 V with a C/10 (2.08 A m^{-2}) constant current (using the same protocol as the two-electrode cycling), and then twice with a C/3 (8.25 A m^{-2}) constant current. After completing the capacity checks, the cells were disconnected from the TOSCAT potentiostat and connected to a Solartron 1280 C potentiostat/frequency response analyser controlled with CORRWARE and ZPLOT software. The cell was electrically connected again as a two-electrode cell, and the cell charged to 4.2 V with a C/3 (8.25 A m^{-2}) constant current, followed by a constant potential (4.2 V) period for 2 h and an open-circuit condition for 7 h. During this OCP period, the reference electrode was prepared *in situ* and the electrical cell connections re-adjusted so that the potential of the working electrode was measured versus the reference electrode. From this state, the impedance measurement routine began. This involved discharging the cell with a C/10 (2.08 A m^{-2}) constant current down to the target voltage and holding the electrode at this potential for 2 h, followed by 2 h at an open-circuit condition. The impedance was then measured potentiostatically at this final OCP potential with a 10 mV perturbation for the frequencies 20 kHz to 1.0 mHz (these frequencies represented the limits of the instrument). The lithium–tin (Sn) reference electrode potential was measured to be 400 mV versus the lithium foil. For convenience, the working electrode potential is reported versus Li/Li$^+$ in this article. The EIS data were acquired at the following potentials representing the target SOCs identified by the GITT data: 4.20 V vs Li/Li$^+$ (SOC 100%), 4.14 V vs Li/Li$^+$ (SOC 80%), 4.09 V vs Li/Li$^+$ (SOC 60%), 4.02 V vs Li/Li$^+$ (SOC 40%) and 3.97 V vs Li/Li$^+$ (SOC 20%).

The tests undertaken on the positive electrode samples were repeated in exactly the same way for the negative electrode samples. The differences were found in the upper and lower voltage limits and the target potentials during the impedance measurements. The negative electrode cells were cycled as a two-electrode cell, with the working electrode cable connected to the graphite electrode, and the counter electrode cable connected to the lithium foil. The cells were cycled twice between 1.5 and 0.01 V with a C/10 (2.08 A m^{-2}) constant current (using the same protocol as the two-electrode cycling), and then twice with a C/3 (8.25 A m^{-2}) constant current. The impedance measurement routine involved holding the electrode at 0.01 V vs Li/Li$^+$ for 1 h, followed by OCP for 2 h. The cell was then charged with a C/10 (2.08 A m^{-2}) constant current to the target potential and held at this potential for 2 h, followed by 2 h at an open-circuit condition. The impedance was then measured potentiostatically at this final OCP potential with a 10 mV perturbation for the frequencies 20 kHz to 1.0 mHz. This routine was repeated to acquire data at potentials representing the target SOCs: 0.01 V vs Li/Li$^+$ (SOC 100%), 0.09 V vs Li/Li$^+$ (SOC 80%), 0.094 V vs Li/Li$^+$ (SOC 60%), 0.13 V vs Li/Li$^+$ (SOC 40%) and 0.16 V vs Li/Li$^+$ (SOC 20%).

3. Results

3.1. Ageing-related degradation of harvested electrodes

Tables 2 and 3 show the capacities of the harvested positive and negative electrode samples, respectively. The impedance data for the various electrodes are shown in Figs. 3, 4 and 7, 8 for the positive and negative electrode samples, respectively. The effect of cycling on the electrochemical response of both the positive and negative electrode was determined by comparing data from fresh electrodes with data from electrodes harvested from pouch cells aged at 25 °C DOD 40% after 1200 and 2200 completed cycles. The effect of temperature was determined by comparing data from electrodes harvested from cells aged at 25 °C DOD 40% and at 45 °C DOD 40% after 1200 completed cycles. Finally, the effect of depth-of-discharge was determined by comparing data from electrodes harvested from cells aged at 45 °C DOD 20% and at 45 °C DOD 40% after 1200 completed cycles.

3.1.1. Positive electrode data

The positive electrode capacity data are shown in Table 2. Fresh electrodes had a capacity that had a small dependence on the current load, whereas the capacity of harvested electrodes for all ageing conditions showed a strong dependence, thus clearly indicating the increase of the electrode impedance with ageing. Further examination of the measured capacities in Table 2 revealed the progressive decrease in the electrode capacity with cycle number, as shown for the harvested electrodes aged at 25 °C DOD 40% and

Table 2
Capacity of harvested positive electrodes measured in a two-electrode pouch cell set-up

Current density [A m^{-2}]	Cycling condition	Capacity [Ah m^{-2}]				
		Fresh [a]	p1 [b]	p2 [c]	p3 [d]	p4 [e]
2.08 (C/10)	Charge	24.1864	22.9474	22.4102	22.3139	20.8532
	% Decrease	–	5.1229	7.3440	7.7421	13.7813
	Discharge	23.9860	22.8484	22.4047	22.2573	20.8560
	% Decrease	–	4.7430	6.5927	7.2071	13.0495
8.25 (C/3)	Charge	23.3392	21.7582	21.3393	21.1873	19.8287
	% Decrease	–	6.7738	8.5686	9.2203	15.0410
	Discharge	23.3050	21.7991	21.3727	21.1708	19.9600
	% Decrease	–	6.4616	8.2912	9.1579	14.3532
9.43 (C/2.7)	Charge	23.3133	21.7398	21.3598	21.1652	19.8405
	% Decrease	–	6.7493	8.3793	9.2137	14.8959
	Discharge	23.2362	21.7111	21.3503	21.1287	19.9431
	% Decrease	–	6.5636	8.1162	9.0700	14.1724
17.68 (C/1.5)	Charge	22.9769	20.9468	20.7522	20.4921	19.0546
	% Decrease	–	8.8355	9.6821	10.8143	17.0706
	Discharge	22.8240	20.9739	20.3388	20.3149	19.0746
	% Decrease	–	8.1061	10.8884	10.9935	16.4273

[a] Cell subjected to formation cycling at room temperature.
[b] 25 °C DOD 40% 1200 completed cycles (~ 13% decrease of 3 Ah cell C/3 discharge capacity).
[c] 25 °C DOD 40% 2200 completed cycles (~ 18% decrease of 3 Ah cell C/3 discharge capacity).
[d] 45 °C DOD 20% 1200 completed cycles (~ 18% decrease of 3 Ah cell C/3 discharge capacity).
[e] 45 °C DOD 40% 1200 completed cycles (~ 24% decrease of 3 Ah cell C/3 discharge capacity).

harvested after 1200 and 2200 completed cycles. Increasing the temperature to 45 °C whilst maintaining the depth-of-discharge at 40% resulted in more than a two-fold increase of the electrode capacity fade after 1200 completed cycles. However, increasing the temperature could not be solely responsible for this dramatic effect since the capacity fade of the 45 °C DOD 20% electrode was smaller. Hence, the combination of a high temperature (45 °C) and a high depth-of-discharge (40%) had a significant impact on the capacity fade of positive electrodes, which corresponded with the 3 Ah cell capacity fade observation [16].

The impedance data for positive electrodes harvested from cells aged under various conditions are shown in Figs. 3 and 4. The data indicated that the positive electrode impedance increased with: (a) increasing number of cycles (compare cyan and green curves), (b) increasing temperature (compare cyan and red curves), and (c) increasing depth-of-discharge (compare blue and red curves). The impedance changes were primarily limited to changes in both the shape and magnitude of the high-frequency semi-circle. In particular, increasing the number of cycles or increasing the temperature for cells aged with DOD 40% led to a significant change in both the shape and magnitude of the high-frequency semi-circle for the low SOCs (20 and 40%) in comparison with the higher SOCs (80 and 100%), which corresponded to both higher intercalated lithium-ion concentrations and the second potential plateau shown in Fig. 2(a). The impact of the different ageing conditions on the change in the high-frequency semi-circle at low SOCs is clearly demonstrated in

Table 3
Capacity of harvested negative electrodes measured in a two-electrode pouch cell set-up

Current density [A m^{-2}]	Cycling condition	Capacity [Ah m^{-2}]				
		Fresh [a]	n1 [b]	n2 [c]	n3 [d]	n4 [e]
2.08 (C/10)	Charge	25.9996	25.0337	24.8235	24.6745	24.6568
	% Decrease	–	3.7152	4.5238	5.0967	5.1647
	Discharge	25.8432	24.8258	24.6140	24.5885	24.5637
	% Decrease	–	3.9369	4.7565	4.8553	4.9511
8.25 (C/3)	Charge	25.8538	24.7496	24.4364	24.4376	24.2450
	% Decrease	–	4.2712	5.4826	5.4780	6.2228
	Discharge	25.7340	24.6054	24.3059	24.4816	24.2328
	% Decrease	–	4.3857	5.5494	4.8668	5.8334
9.43 (C/2.7)	Charge	25.7835	24.6722	24.3244	24.2155	24.1255
	% Decrease	–	4.3103	5.6591	6.0813	6.4303
	Discharge	25.6994	24.4816	24.1589	24.3633	24.0882
	% Decrease	–	4.7387	5.9942	5.1990	6.2694
17.68 (C/1.5)	Charge	25.7167	24.4108	24.1393	23.7636	23.7388
	% Decrease	–	5.0779	6.1338	7.5946	7.6909
	Discharge	25.5163	24.3743	23.9911	23.7282	23.7039
	% Decrease	–	4.4755	5.9771	7.0074	7.1029

[a] Cell subjected to formation cycling at room temperature.
[b] 25 °C DOD 40% 1200 completed cycles [~ 13% decrease of 3 Ah cell C/3 discharge capacity).
[h] 25 °C DOD 40% 2200 completed cycles [~ 18% decrease of 3 Ah cell C/3 discharge capacity).
[d] 45 °C DOD 20% 1200 completed cycles [~ 18% decrease of 3 Ah cell C/3 discharge capacity).
[e] 45 °C DOD 40% 1200 completed cycles [~ 24% decrease of 3 Ah cell C/3 discharge capacity).

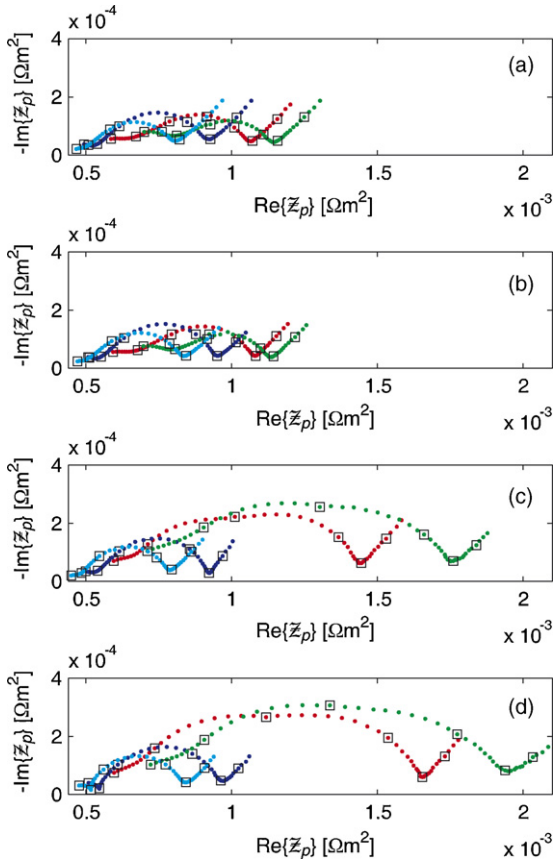

Fig. 3. Positive electrode impedance results from 20 kHz to 0.1 Hz: (a) SOC 100% (4.20 V vs Li/Li$^+$), (b) SOC 80% (4.14 V vs Li/Li$^+$), (c) SOC 40% (4.02 V vs Li/Li$^+$), (d) SOC 20% (3.97 V vs Li/Li$^+$); (●) 25 °C DOD 40% 1200 cycles, (●) 25 °C DOD 40% 2200 cycles, (●) 45 °C DOD 20% 1200 cycles, (●) 45 °C DOD 40% 1200 cycles. Each decade in frequency (20 kHz, 2 kHz, 200 Hz, 20 Hz, 2 Hz, 200 mHz) indicated with □ (For interpretation of the references to colour in this figure legend, the reader is referred to the web version of the article).

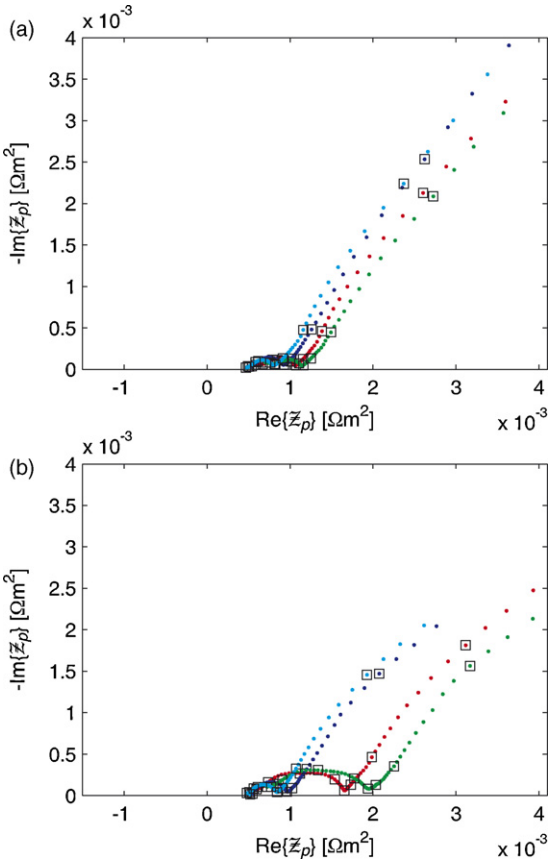

Fig. 4. Positive electrode impedance results from 20 kHz to 1.0 mHz: (a) SOC 100% (4.20 V vs Li/Li$^+$), (b) SOC 20% (3.97 V vs Li/Li$^+$); (●) 25 °C DOD 40% 1200 cycles, (●) 25 °C DOD 40% 2200 cycles, (●) 45 °C DOD 20% 1200 cycles, (●) 45 °C DOD 40% 1200 cycles. Each decade in frequency (20 kHz, 2 kHz, 200 Hz, 20 Hz, 2 Hz, 200 mHz, 20 mHz, 2 mHz) indicated with □ (For interpretation of the references to colour in this figure legend, the reader is referred to the web version of the article).

Fig. 3(c) and (d). Attempts to reduce this significant change in the high-frequency semi-circle by increasing the pressure applied to the pouch cell did not have an effect. Furthermore, the observed high-frequency behaviour was accompanied with an increase in the magnitude of the low-frequency impedance, as shown in Fig. 4(b). In addition to the changes in both the shape and magnitude of the high-frequency semi-circle, an increase in the high-frequency real axis intercept was observed and could be attributable to either an effect of ageing or an artefact of harvested electrode assembly.

In addition to observing changes in the magnitude of the impedance as a function of cycle number under different testing temperatures and depths-of-discharge, it was important to investigate any shifts in the frequency at which different characteristic features of the Nyquist plot were observed. In particular, a possible change in the frequency at which the intersection between the high-frequency semi-circle and the low-frequency diffusion tail, defined as *fmin* in other work [21], was examined. Each decade change of frequency is indicated in Figs. 3 and 4, with the frequency of *fmin* observed to remain the same regardless of the testing condition or cycle number.

After observing the significant change in the high-frequency semi-circle at low SOCs for two of the ageing cases, the C/10 (2.08 A m^{-2}) cycling curves were examined and shown in Fig. 5. The curves were normalised in order to observe differences in the cycling behaviour between the fresh and aged cases, with the results for the two cells showing both the lowest (25 °C DOD 40% 1200 cycles) and highest (45 °C DOD 40% 1200 cycles) degree of performance degradation shown in Fig. 5(a) and (b), respectively. The positive electrodes harvested from cells aged for 1200 cycles at 25 °C DOD 40% did not show a significant change in the high-frequency semi-circle at low SOCs, with no significant changes observed in the cycling behaviour. However, the positive electrodes harvested from the cells that did show a significant change in the high-frequency semi-circle at low SOCs did exhibit a significant change in the cycling behaviour. In particular, a noticeable change was observed in the potential range corresponding to the second potential plateau in Fig. 2(a) and hence corresponding to the SOCs where significant changes were observed in the high-frequency semi-circle of the measured impedance.

3.1.2. Negative electrode data

An investigation of the measured capacities in Table 3 revealed that fresh electrodes had a capacity which was essentially independent of the current load, whereas the capacity of harvested electrodes for all ageing conditions showed a dependence on the current load, thus clearly indicating the increase of the electrode impedance with ageing. Further examination of the measured capacities in Table 3 revealed only a small progressive decrease in the electrode capacity with cycle number, as shown for the harvested electrodes aged at 25 °C DOD 40% and harvested after 1200 and 2200 completed cycles. Increasing the temperature to 45 °C whilst maintaining the depth-of-discharge at 40% resulted in a further approximately 50% increase of the electrode capac-

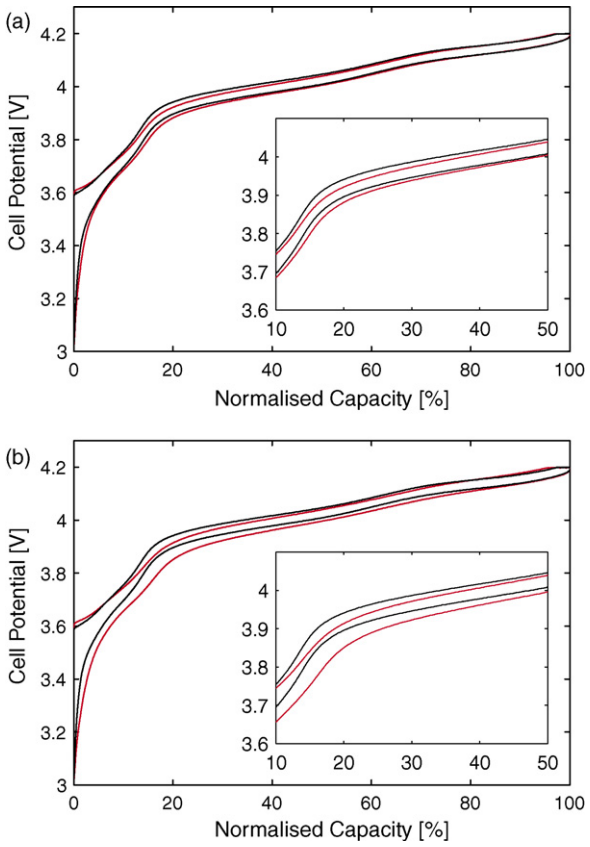

Fig. 5. C/10 (2.08 A m^{-2}) cycling (3.0–4.2 V) of positive electrodes; (–) fresh, (▬) aged: (a) 25 °C DOD 40% 1200 cycles, (b) 45 °C DOD 40% 1200 cycles (For interpretation of the references to colour in this figure legend, the reader is referred to the web version of the article).

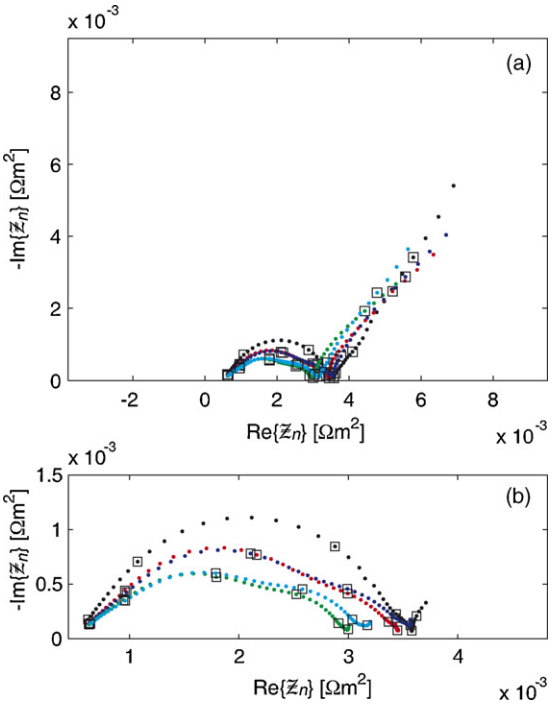

Fig. 6. Negative electrode impedance results for a fresh electrode: (a) 20 kHz to 1.0 mHz, (b) 20 kHz to 0.1 Hz; (●) SOC 100% (0.01 V vs Li/Li$^+$), (●) SOC 80% (0.09 V vs Li/Li$^+$), (●) SOC 60% (0.094 V vs Li/Li$^+$), (●) SOC 40% (0.13 V vs Li/Li$^+$), (●) SOC 20% (0.16 V vs Li/Li$^+$). Each decade in frequency (20 kHz, 2 kHz, 200 Hz, 20 Hz, 2 Hz, 200 mHz) indicated with □ (For interpretation of the references to colour in this figure legend, the reader is referred to the web version of the article).

ity fade after 1200 completed cycles. Furthermore, decreasing the depth-of-discharge to 20% at 45 °C resulted in a similar decrease in capacity.

The impedance of both fresh and harvested negative electrodes was measured, however, the samples aged at 45 °C DOD 20% for 1200 completed cycles and 25 °C DOD 40% for 2200 completed cycles failed after two attempts to construct three-electrode pouch cells. A comparison of the measured impedance spectra for the fresh electrode with harvested electrodes at all SOCs, see Figs. 6–8 , revealed that the magnitude of the high-frequency semi-circle for the fresh electrode was larger, perhaps indicating wetting problems. In addition, the magnitude of the high-frequency impedance semi-circle was much larger for the fresh negative electrode than the fresh positive electrode (compare Figs. 9 and 6). The difference in magnitudes was preliminarily investigated with model simulations. Using a previously developed physically based impedance model (with all incorporated effects of ageing switched off) [22], both electrodes were simulated with manufacturer-provided particle sizes (similar in both cases), porosities (similar in both cases) and electrode thicknesses (significantly different), assuming: similar electrode kinetics, double-layer capacitances and solid-phase diffusion coefficients. The simulated electrode impedances revealed that the difference in negative and positive electrode impedances could be primarily attributed to differing electrode geometries. The assumptions used for the simulations would need to be investigated with modelling fitting, similar in nature to previous work [18].

A comparison of data from the 25 °C DOD 40% and 45 °C DOD 40% samples indicated that the negative electrode impedance rise was higher at the higher ageing temperature. The impedance changes were located primarily in the high-frequency region, with a change both in the width of the high-frequency semi-circle and the magnitude of the high-frequency intercept. Examination of the frequencies at which different features of the Nyquist plot were observed (each decade change indicated in Figs. 7 and 8) indicated no change regardless of the testing condition. The cycling behaviour of fresh and aged negative electrodes was examined with normalised C/10 (2.08 A m^{-2}) capacity curves, shown in Fig. 10. No significant changes were observed in the cycling behaviour of any of the aged electrodes, indicating that the graphite active material had maintained its structural integrity.

4. Discussion

Electrochemical measurements of electrodes harvested from aged 3 Ah pouch cells led to the identification of the positive electrode as having a larger capacity fade for all ageing cases and at all current loads. Similar lifetime work on $Li_xMn_2O_4$/Li_xC_6 lithium-ion cells has also identified the positive electrode as having a noticeably larger decrease in capacity, attributed primarily to a decrease in rate capability in the second potential plateau [23,24]. This identification of the increase in resistance during lithiation in the second potential plateau corresponds well with the observation in this study of the dependence of the electrode impedance on the SOC. This observation had a unique implication for proposed ageing mechanisms, in the sense that the effect of ageing had to result in a significantly larger high-frequency semi-circle at higher solid-phase lithium-ion concentrations.

The degradation of positive electrodes in 4 V $Li_xMn_2O_4$-based cells has been extensively studied in a variety of test matrices, with factors such as synthesis conditions [25,26], cation

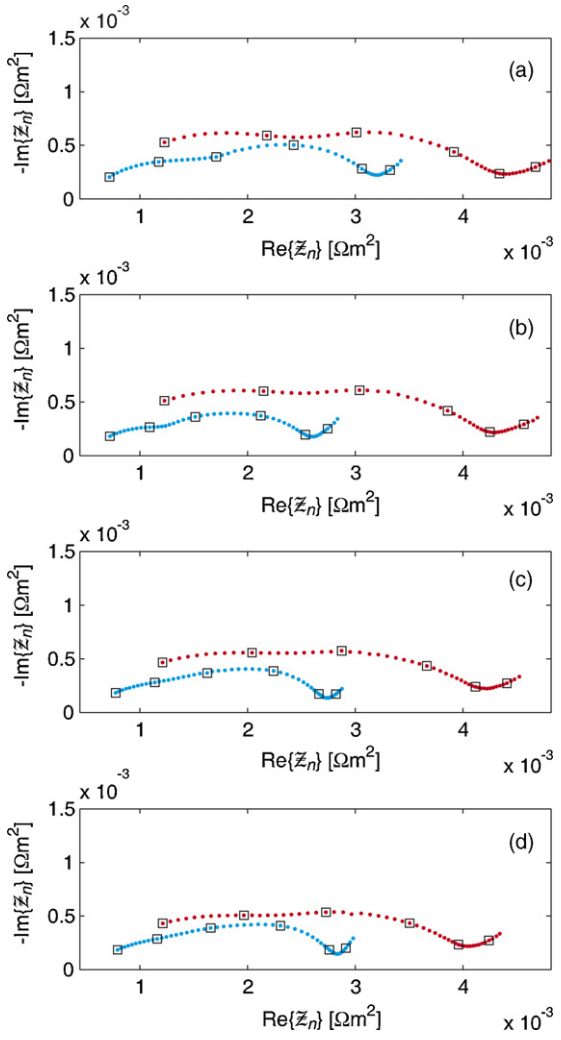

Fig. 7. Negative electrode impedance results from 20 kHz to 0.1 Hz: (a) SOC 100% (0.01 V vs Li/Li$^+$), (b) SOC 80% (0.09 V vs Li/Li$^+$), (c) SOC 40% (0.13 V vs Li/Li$^+$), (d) SOC 20% (0.16 V vs Li/Li$^+$); (●) 25 °C DOD 40% 1200 cycles, (●) 45 °C DOD 40% 1200 cycles. Each decade in frequency (20 kHz, 2 kHz, 200 Hz, 20 Hz, 2 Hz, 200 mHz) indicated with □ (For interpretation of the references to colour in this figure legend, the reader is referred to the web version of the article).

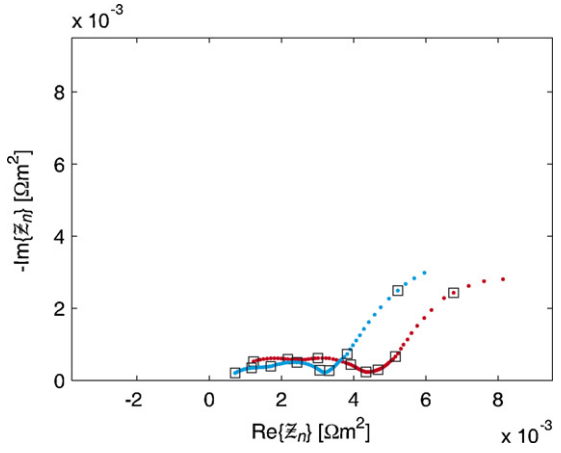

Fig. 8. Negative electrode impedance results from 20 kHz to 1.0 mHz; SOC 100% (0.01 V vs Li/Li$^+$); (●) 25 °C DOD 40% 1200 cycles, (●) 45 °C DOD 40% 1200 cycles. Each decade in frequency (20 kHz, 2 kHz, 200 Hz, 20 Hz, 2 Hz, 200 mHz) indicated with □ (For interpretation of the references to colour in this figure legend, the reader is referred to the web version of the article).

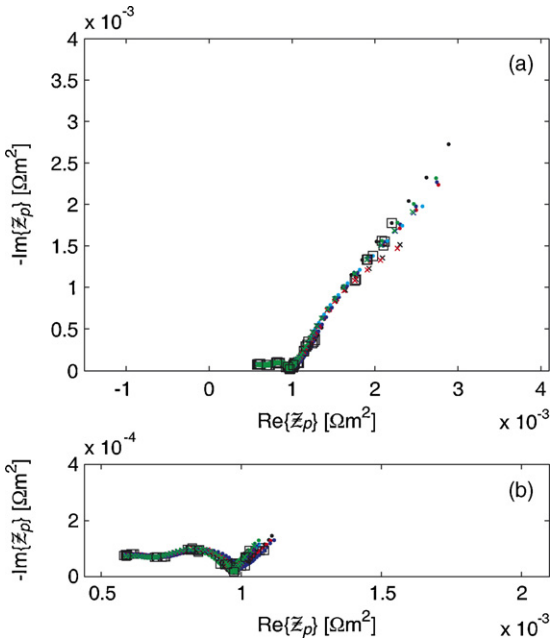

Fig. 9. Positive electrode impedance results for a fresh electrode: (a) 20 kHz to 1.0 mHz, (b) 20 kHz to 0.1 Hz; (•) SOC 100% (4.20 V vs Li/Li$^+$), (●) SOC 80% (4.14 V vs Li/Li$^+$), (●) SOC 60% (4.09 V vs Li/Li$^+$), (●) SOC 40% (4.02 V vs Li/Li$^+$), (●) SOC 20% (3.97 V vs Li/Li$^+$). Each decade in frequency (20 kHz, 2 kHz, 200 Hz, 20 Hz, 2 Hz, 200 mHz) indicated with □ (For interpretation of the references to colour in this figure legend, the reader is referred to the web version of the article).

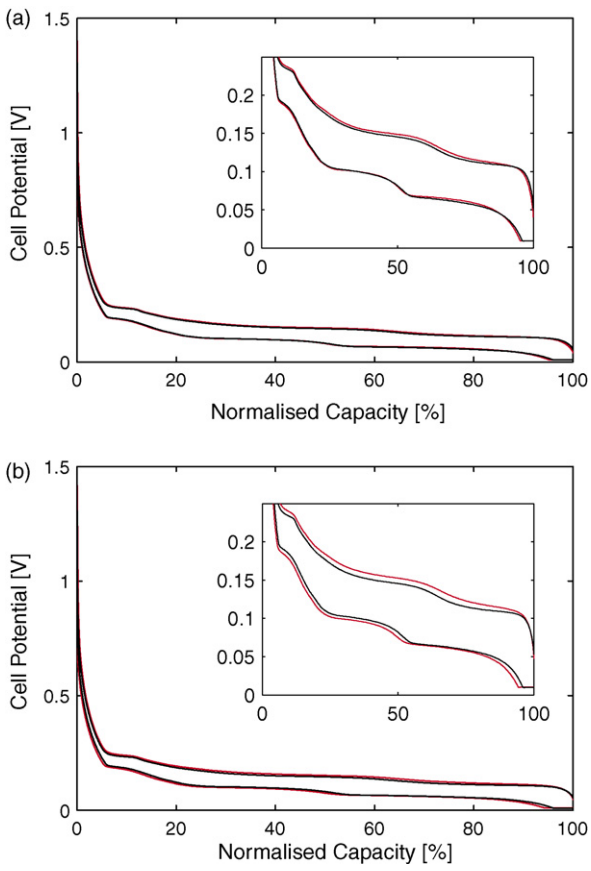

Fig. 10. C/10 (2.08 A m^{-2}) cycling (0.01–1.5 V) of negative electrodes; (–) fresh, (—) aged: (a) 25 °C DOD 40% 1200 cycles, (b) 45 °C DOD 40% 1200 cycles (For interpretation of the references to colour in this figure legend, the reader is referred to the web version of the article).

and oxygen stoichiometry [27,28], cycling rates [15,23,26,29,30], depth-of-discharge (particularly larger DODs) [11,28], temperature [11,23,27,28,31], type and concentration of salt [11,23,32,33], type of solvent [32], type and concentration of impurities (e.g., HF and H_2O) [31,34–36], electrode morphology [27,31,37] and manganese oxidation state [27,28,38] all found to have an effect. The processes proposed as sources of electrode degradation in $Li_xMn_2O_4$ include: (1) solubility of the spinel electrode in the electrolyte. The solubility has been attributed to acid (i.e., HF contained in the electrolyte) attack and a disproportionation of Mn^{3+} at the particle surface [12,39,40], however, some experiments have found no correlation between the amount of dissolved manganese and the capacity fade [11,33,41], (2) degradation of the particle surface due to non-equilibrium conditions during discharge, resulting in the onset of a Jahn–Teller effect and the formation of a Mn^{3+}-rich tetragonal phase ($Li_2Mn_2O_4$) that would damage structural integrity and particle-to-particle contact [13,15,26], (3) a combination of (1) and (2), transforming the surface of the particles into defect spinels (e.g., $Li_2Mn_4O_9$) plus Li_2MnO_3[23,42]; these phases were detected in XRD measurements [24,42], (4) accumulation of λ-MnO_2 upon charging, resulting in an abrupt contraction of the lattice and leading to reduced electrical contact [29,32], (5) solvent oxidation at high potentials when charging the cells, especially at slow rates due to the sluggish kinetics between 3.5 and 4.5 V vs Li/Li^+[30,43], which could lead to loss of oxygen from the host structure [44] or production of Lewis acids [32] resulting in manganese dissolution [30], and (6) combination of the previous five processes, with electrolyte degradation/solvent oxidation generating acid species which leads to the dissolution of manganese and formation of a deficient spinel, that changes to a λ-MnO_2 phase in the presence of H^+, which furthermore becomes protonated and only partially intercalates lithium-ions [32].

In addition to the SOC-dependence of the measured positive electrode impedance, there were two further important observations from the three-electrode positive impedance measurements which assisted in evaluating which ageing hypothesis was most plausible. Firstly, increasing the temperature simply decreased the time required for an effect of ageing to be observed, hence indicating that the ageing mechanism was the same both at room and elevated temperatures which has also been observed in other work [28]. Secondly, significant changes in the high-frequency impedance semi-circle were observed for electrodes cycled in DOD 40% cells, where twice the current (2.0 A) was used to withdraw 40% of the cell capacity in 35 min which could lead to significant solid-phase lithium-ion concentration gradients in the active particles that were $> 20\,\mu m$ in diameter. The importance of depth-of-discharge has been observed in other work, with the rate of electrode degradation accelerated at higher DODs [11,28]. It has been proposed that under dynamic conditions above 3 V, the surface of some active particles may reach the stoichiometric spinel composition, $LiMn_2O_4$, resulting in the onset of a Jahn–Teller effect and thereby transforming the surface into a Mn^{3+}-rich $Li_{1+x}[Mn_2O_4]$ region [13,15]. The structural degradation of the positive active material surface alone does not account for the increase in both the capacity fade and impedance at higher temperatures, since the Jahn–Teller effect scales inversely with temperature [28] and the solid-phase lithium-ion diffusion coefficient approximately follows the Arrhenius equation [45]. Instead, it is necessary to consider both the observed importance of active surface area [27] and the thermal degradation of $LiPF_6$-based electrolytes [34,36,46,47] on the observed electrode degradation at elevated temperatures, and conclude that the overall mechanism probably includes manganese dissolution due to acid (HF) attack and a disproportionation reaction at the particle surface [12,39,40]. The general view in the literature is that manganese dissolution coupled with surface phase transitions at high intercalated lithium-ion concentrations leads to a resistive and potentially electrochemically inactive degraded solid-phase (with or without protonation), that increases in thickness with a shrinking core model. The remaining question is how does this degraded surface affect the impedance, and can the dependence on the solid-phase lithium-ion concentration be justified.

There are four possible SOC-dependent scenarios based on a degraded active surface that could potentially give the required high-frequency semi-circle behaviour. Firstly, it has been proposed that the formation of a tetragonal $Li_2Mn_2O_4$ surface species would result in electromechanical grinding [28] and damage both active/conductive carbon and active/active contact, resulting in particle isolation. A reduction of the number of particles would decrease the surface area available for faradaic reaction, hence resulting in an increase of the high-frequency semi-circle. In addition, particles that did not become completely isolated would experience an increase in the local contact resistance which would depend on the state-of-charge of the active material. A similar ageing hypothesis has been recently proposed for nickelate-based positive electrodes [18]. As is the case for nickelate-based materials, the volume of manganese spinel particles increases upon lithiation [48]. However, the contact pressure between particles should be higher at larger solid-phase lithium-ion concentrations, hence this ageing scenario is unlikely solely responsible for the observed high-frequency semi-circle behaviour.

Secondly, the degraded surface layer results in a resistance through which the local active current (faradaic plus double-layer) must pass, with the electronic conductivity of the surface layer dependent on the lithium-ion concentration (i.e., oxidation state of the manganese). A similar ageing hypothesis has also been proposed for nickelate-based positive electrodes, where the formation of a rock-salt structured surface $Li_xNi_{1-x}O$ layer with a potentially lower electronic conductivity at lower lithium-ion concentrations results in a SOC-dependent resistance [49]. An increase in the local resistance coupled with the double-layer current of the conductive carbon would result in an increase of the high-frequency semi-circle [18,22]. It is difficult to evaluate this hypothesis since there is evidence of different Li–Mn–O phases present on the surface of active particles in aged positive electrodes [13,15,23,24,26,42] and limited data available on the electronic conductivity of such layers. The effective charge carriers are electrons (polarons) that have a mobility dependent on the activation energy needed to provide the energetic equivalency of the donor (Mn^{3+}) and acceptor (Mn^{4+}) sites [50,51]. Density functional theory investigation of the electronic structure of mixed valent $Li_xMn_2O_4$ spinels concluded that small deviations (x) from stoichiometry ($Li_{1+x}Mn_2O_4$, $x > 0$ or $x < 0$, depending on preparation conditions) lead to drastic changes in the structure and electronic properties [50]. In the case that the degraded surface layer consists of Li_2MnO_3, a manganese oxidation state of 4+ results in electrochemical inactivity because the Mn^{4+} ion cannot be easily oxidised to the Mn^{5+} state [23,52]. In addition, the inability to oxidise the Mn^{4+} ions renders this spinel phase electronically insulating. The alternative/additional defect spinel phase, $Li_2Mn_4O_9$, also has a very limited capacity in the positive electrode potential window [23]. Therefore, it is reasonable to conclude that the degraded surface layer can be viewed solely as a lithium-ion conductor that has a resistance independent of the bulk phase intercalated lithium-ion concentration, hence this hypothesis can be tentatively dismissed.

The final two possible scenarios relate to the kinetics of the faradaic reaction, which has also been suggested as the sole source of both impedance increase and capacity fade in other work [30]. The difference between the two scenarios is where the faradaic reaction is considered to occur. If the faradaic reaction is viewed as

occurring at the interface between the degraded surface layer and the electrolyte, the structural characteristics of the degraded surface layer could cause a different SOC-dependent exchange current density. A decrease in the exchange current density would result in an increase of the high-frequency semi-circle [53]. However, if the degraded surface layer is viewed solely as a lithium-ion conductor similar in nature to the solid-electrolyte interface (SEI) on the negative electrode, the faradaic reaction is then viewed as occurring at the interface between the bulk manganese spinel phase and the degraded surface layer. A change in the structural properties of the bulk manganese spinel phase could cause a different SOC-dependent exchange current density. Support for this hypothesis is provided by the low-current (C/10) normalised capacity results, where a clear change was observed in the cycling behaviour, hence possibly indicating a bulk structural change of the spinel phase. Further support is provided by the increase of the magnitude of the low-frequency impedance, perhaps indicating a structurally based change of the solid-phase diffusion coefficient. In order to determine which of the above scenarios is correct, harvested electrode samples would need to be investigated with material characterisation techniques that allowed for the investigation of the SOC-dependence of both the solid-phase conductivity and the lattice parameters (e.g., *in situ* XRD [54]).

The focus thus far has been on the positive electrode, however, subtle changes in the capacity and impedance of the negative electrode require attention. Although the capacity fade of the positive electrode was found to be larger in comparison with the negative electrode both at all current loads and ageing conditions, the percentage decrease was less than the overall cell (3 Ah) capacity fade. Factors that can affect the effective capacity, operating window and cycle path of lithium-ion cells include: (1) loss of active material, (2) loss of cycleable lithium, and (3) relative shifts in electrode SOC-windows [55,56]. A recent study highlighted the complicated nature of the capacity fade of $Li_xMn_2O_4$-based cells, with the combination of the formation of defect spinels at the positive electrode with manganese reduction at the negative electrode contributing to a presence of all three capacity fade factors [56]. In order to distinguish between the magnitude of the contributions of loss of cycleable lithium and relative shifts in electrode SOC-windows, a reference electrode would need to be incorporated into the 3 Ah cells. Observed changes in the width and shape of the high-frequency semi-circle for negative electrodes could potentially be attributed to the continual break-down and reformation of a protective surface layer on the graphite and/or copper current collector, consuming cycleable lithium ions. An increase in the high-frequency real axis intercept could be attributable to either an effect of ageing or an artefact of harvested electrode assembly. In addition, the self-discharge observed for the 3 Ah cells [16] could be attributed to a corrosion reaction with a mixed potential at the negative electrode, resulting in delithiation and an increase in the electrode potential [24].

5. Conclusions

The low-earth-orbit cycle life performance of commercial 3 Ah laminated $Li_xMn_2O_4$-based lithium-ion batteries has been investigated in a matrix of different cycling DODs (0, 20, 40%) and temperatures (25, 45 °C). Aged cells were disassembled and the electrochemical performance of harvested electrodes investigated with both two- and three-electrode pouch cells. The following points summarise the main conclusions of this study:

(1) The specially designed three-electrode pouch cell incorporating a tin reference electrode was truly an enabling technology. The use of a pouch cell configuration was invaluable with respect to both applying and maintaining a reasonable pressure on the electrode assembly. In addition, the size and position of the reference electrode did not significantly impact on the current distribution, hence allowing the attainment of both high quality and highly reproducible impedance data.
(2) Harvested positive electrodes were identified as having a larger capacity fade in comparison with the negative electrodes for all ageing cases and at all current loads.
(3) The measured impedance spectra for both harvested positive and negative electrodes at all ageing conditions revealed that changes were primarily located in the high-frequency semi-circle. In addition, changes in the magnitude of the high-frequency semi-circle for the 3 Ah cells at low SOCs could be attributed to the positive electrode. Cycling 3 Ah cells for extended periods of time or at higher temperatures with a 40% depth-of-discharge led to a significant change in both the shape and magnitude of the positive electrode high-frequency semi-circle at low SOCs (20 and 40%), which corresponded to both higher intercalated lithium-ion concentrations and the second potential plateau for $Li_xMn_2O_4$.
(4) Low-current (C/10) cycling of harvested positive electrodes revealed that cells which exhibited a significant increase in the high-frequency semi-circle at low SOCs had a corresponding change in the cycling behaviour. It was postulated that structural degradation of the spinel phase present in the second potential plateau for $Li_xMn_2O_4$ resulted in a change of the electrode kinetics, hence impacting on the magnitude of the high-frequency semi-circle at the corresponding SOCs.
(5) Harvested positive and negative electrodes for all ageing conditions exhibited a noticeable increase in the high-frequency real axis intercept, perhaps attributable to either an effect of ageing or an artefact of the harvested electrode assembly. However, the increase in the high-frequency real axis intercept correlated with the same observation for the 3 Ah cells.
(6) Subtle changes were observed in the discharge capacity and impedance of harvested negative electrodes, with a SOC-independent increase in the width of the high-frequency semi-circle.
(7) Loss of active material from either electrode was not solely responsible for the observed 3 Ah cell capacity fade. A combination of a loss of active material, cycleable lithium and a shift in SOC operating windows was deemed responsible, with the contribution of each only discernable with an extension of the lifetime matrix to include 3 Ah cells with an internally calibrated reference electrode.
(8) The 3 Ah cell performance was adequate for short-term 'piggyback' LEO satellite missions. However, lifetime performance would need to be improved for either longer term or higher temperature missions.

Overall, the three-tiered approach to battery lifetime studies, including: (1) terrestrial and orbital comparison [16], (2) terrestrial lifetime studies, and (3) electrochemical examination of harvested aged electrodes with two- and three-electrode pouch cells, provided a solid foundation for the evaluation of this battery chemistry.

Acknowledgements

Financial support from the Japan Aerospace Exploration Agency (JAXA) is gratefully acknowledged. Shelley Brown would like to thank Yoshitsugu Sone, Keita Ogawa and Masatoshi Uno for providing the resources and support necessary to undertake the lifetime work at JAXA.

References

[1] X. Wang, C. Yamada, H. Naito, S. Kuwajima, J. Power Sources 140 (2005) 129.
[2] R.A. Marsh, S. Vukson, S. Surampudi, B.V. Ratnakumar, M.C. Smart, M. Manzo, P.J. Dalton, J. Power Sources 97–98 (2001) 25.
[3] J.P. Fellner, G.J. Loeber, S.P. Vukson, C.A. Riepenhoff, J. Power Sources 119–121 (2003) 911.
[4] Y. Sone, X. Liu, T. Inoue, X. Wang, S. Kuwajima, Electrochemistry (Tokyo Jpn.) 71 (2003) 542.
[5] H. Yoshida, N. Imamura, T. Inoue, K. Komada, Electrochemistry (Tokyo Jpn.) 71 (2003) 1018.
[6] M.C. Smart, B.V. Ratnakumar, L.D. Whitcanack, K.B. Chin, S. Surampudi, R. Gitzendanner, F. Puglia, J. Byers, IEEE AESS Systems Magazine 19 (2004) 18.
[7] X. Wang, Y. Sone, S. Kuwajima, J. Power Sources 142 (2005) 313.
[8] X. Wang, Y. Sone, H. Naito, C. Yamada, G. Segami, K. Kibe, J. Power Sources 161 (2006) 594.
[9] B. McKissock, C. Reid, M. Manzo, T. Miller, D. Britton, W. Bennett, in: M., Anderman (Ed.), Second International Symposium on Large Lithium Ion Battery Technology and Application (2006).
[10] X. Wang, Y. Sakiyama, Y. Takahashi, C. Yamada, H. Naito, G. Segami, T. Hironaka, E. Hayashi, K. Kibe, J. Power Sources 167 (2007) 162.
[11] T. Inoue, M. Sano, J. Electrochem. Soc. 145 (1998) 3704.
[12] M.M. Thackeray, P.J. Johnson, L.A. de Picciotto, P.G. Bruce, J.B. Goodenough, Mater. Res. Bull. 19 (1984) 179.
[13] M.M. Thackeray, J. Electrochem. Soc. 142 (1995) 2558.
[14] M.M. Thackeray, W.I.F. David, P.G. Bruce, J.B. Goodenough, Mater. Res. Bull. 18 (1983) 461.
[15] M.M. Thackeray, Y. Shao-Horn, A.J. Kahaian, K.D. Kepler, E. Skinner, J.T. Vaughey, S.A. Hackney, Electrochem. Solid-State Lett. 1 (1998) 7.
[16] S. Brown, K. Ogawa, Y. Kumeuchi, S. Enomoto, M. Uno, Y. Sone, D. Abraham, G. Lindbergh, J. Power Sources 185 (2008) 1444.
[17] E. Barsoukov, J.R. Macdonald (Eds.), Impedance Spectroscopy; Theory, Experiment, and Applications, second ed., John Wiley & Sons, 2005.
[18] S. Brown, N. Mellgren, M. Vynnycky, G. Lindbergh, J. Electrochem. Soc. 155 (2008) A320.
[19] D.P. Abraham, S.D. Poppen, A.N. Jansen, J. Liu, D.W. Dees, Electrochim. Acta 49 (2004) A4763.
[20] W.A. van Schalkwijk, B. Scrosati (Eds.), Advances in Lithium-Ion Batteries, first ed., Kluwer Academic/Plenum Publishers, 2002.
[21] D.P. Abraham, E.M. Reynolds, P.L. Schultz, A.N. Jansen, D.W. Dees, J. Electrochem. Soc. 153 (2006) A1610.
[22] N. Mellgren, S. Brown, M. Vynnycky, G. Lindbergh, J. Electrochem. Soc. 155 (2008) A304.
[23] A.D. Robertson, S.H. Lu, W.F. Howard Jr., J. Electrochem. Soc. 144 (1997) 3505.
[24] A. Blyr, C. Sigala, G. Amatucci, D. Guyomard, Y. Chabre, J.-M. Tarascon, J. Electrochem. Soc. 145 (1998) 194.
[25] G. Pistoia, G. Wang, Solid State Ionics 66 (1993) 135.
[26] W. Liu, K. Kowal, G.C. Farrington, J. Electrochem. Soc. 143 (1996) 3590.
[27] G.G. Amatucci, C.N. Schmutz, A. Blyr, C. Sigala, A.S. Godz, D. Larcher, J.M. Tarascon, J. Power Sources 69 (1997) 11.
[28] G.G. Amatucci, N. Pereira, T. Zheng, J.-M. Tarascon, J. Electrochem. Soc. 148 (2001) A171.
[29] H. Huang, C.A. Vincent, P.G. Bruce, J. Electrochem. Soc. 146 (1999) 3649.
[30] D. Aurbach, M.D. Levi, K. Gamulski, B. Markovsky, G. Salitra, E. Levi, U. Heider, L. Heider, R. Oesten, J. Power Sources 81–82 (1999) 472.
[31] G.G. Amatucci, A. Blyr, C. Sigala, P. Alfonse, J.M. Tarascon, Solid State Ionics 104 (1997) 13.
[32] A. du Pasquier, A. Blyr, P. Courjal, D. Larcher, G. Amatucci, B. Gérand, J.-M. Tarascon, J. Electrochem. Soc. 146 (1999) 428.
[33] T. Aoshima, K. Okahara, C. Kiyohara, K. Shizuka, J. Power Sources 97–98 (2001) 377.
[34] C.L. Campion, W. Li, B.L. Lucht, J. Electrochem. Soc. 152 (2005) A2327.
[35] L. Yang, M. Takahashi, B. Wang, Electrochim. Acta 51 (2006) 3228.
[36] W. Li, B.L. Lucht, J. Power Sources 168 (2007) 258.
[37] T. Kakuda, K. Uematsu, K. Toda, M. Sato, J. Power Sources 167 (2007) 499.
[38] R.J. Gummow, A. de Kock, M.M. Thackeray, Solid State Ionics 69 (1994) 59.
[39] J.C. Hunter, J. Solid State Chem. 39 (1981) 142.
[40] W. Choi, A. Manthiram, J. Electrochem. Soc. 153 (2006) A1760.
[41] Y. Shin, A. Manthiram, Electrochem. Solid-State Lett. 5 (2002) A55.
[42] J. Cho, M.M. Thackeray, J. Electrochem. Soc. 146 (1999) 3577.
[43] D. Aurbach, B. Markovsky, G. Salitra, E. Markevich, Y. Talyossef, M. Koltypin, L. Nazar, B. Ellis, D. Kovacheva, J. Power Sources 165 (2007) 491.
[44] Y. Gao, J.R. Dahn, Solid State Ionics 84 (1996) 33.
[45] A.-K. Hjelm, T. Eriksson, G. Lindbergh, Electrochim. Acta 48 (2002) 171.
[46] C.L. Campion, W. Li, W.B. Euler, B.L. Lucht, B. Ravdel, J.F. DiCarlo, R. Gitzendanner, K.M. Abraham, Electrochem. Solid-State Lett. 7 (2004) A194.
[47] W. Li, B.L. Lucht, J. Electrochem. Soc. 153 (2006) A1617.
[48] J. Christensen, J. Newman, J. Electrochem. Soc. 153 (2006) A1019.
[49] D. Dees, E. Gunen, D. Abraham, A. Jansen, J. Prakash, J. Electrochem. Soc. 152 (2005) A1409.
[50] M. Atanasov, J.-L. Barras, L. Benco, C. Daul, J. Am. Chem. Soc. 122 (2000) 4718.
[51] J. Molenda, K. Świerczek, M. Molenda, J. Marzec, Solid State Ionics 135 (2000) 53.
[52] S.-H. Park, Y. Sato, J.-K. Kim, Y.-S. Lee, Mater. Chem. Phys. 102 (2007) 225.
[53] M. Doyle, J.P. Meyers, J. Newman, J. Electrochem. Soc. 147 (2000) 99.
[54] T. Eriksson, A.-K. Hjelm, G. Lindbergh, T. Gustafsson, J. Electrochem. Soc. 149 (2002) A1164.
[55] J. Christensen, J. Newman, J. Electrochem. Soc. 150 (2003) A1416.
[56] J. Christensen, J. Newman, J. Electrochem. Soc. 152 (2005) A818.